International Journal for Housing Science and Its Applications
Publish August 10, 2025. Volume 46, Issue 4 Pages 2751-2772

https://doi.org/10.70517/ijhsa464229

Numerical simulation of debris flow movement and accumulation processes based on particle flow theory

Shuyu Jin[1], Lei Wu[1], Li Xie[1], Yaogang Dong[1], Jun Yang[1,*] and Luoxuan Qu[2]
[1] Institute of Geological Hazards Prevention, Gansu Academy of Sciences, Lanzhou, Gansu, 730000, China
[2] School of Earth Sciences, Hebei University of Geosciences, Shijiazhuang, Hebei, 050031, China
Corresponding authors: (e-mail: jsywy0523@163.com).

Abstract Studying the movement process of debris flows is of great significance for predicting their disaster-causing range and implementing reasonable prevention and control measures. The dynamic characteristics of debris flows are complex and variable, and their movement process often involves large deformation issues. When using traditional grid-based numerical methods for calculation, it is easy to cause grid distortion and twisting problems. Therefore, this study adopts the Smooth Particle Hydrodynamics (SPH) method to model the movement and deposition process of debris flows. To validate the proposed method, numerical simulations of debris flow movement and deposition processes were conducted using small-scale model channels and debris flow experiments in small streams. The results showed that the HBP constitutive model effectively fitted the measured rheological properties of the fluid, and the numerical simulation results slightly preceded those of the Cross and Bingham models during the initial stage of fluid movement, demonstrating higher accuracy. The constructed structures hindered the movement of the debris flow, reducing the peak flow velocity at the gully mouth by 0.97 m/s. That is, the constructed structures delayed the movement of the debris flow, reduced its velocity, caused the leading edge of the debris flow fluid to accumulate in advance, and reduced the extent of the debris flow. The study provides a theoretical basis for predicting the movement path and disaster-causing range of debris flows.

Index Terms smooth particle dynamics method, HBP constitutive model, debris flow movement and deposition, numerical simulation

I. Introduction

Mudslides, as a sudden natural disaster, have had a significant impact on human society and the natural environment. They occur when loose materials on mountain slopes or hillsides, under the influence of water, form a high-density mixture that rapidly slides down the slope, converging in gullies and moving downward. This phenomenon lies between the gravitational movement of masses and the hydraulic movement of liquids, exhibiting either viscous laminar flow or dilute turbulent flow characteristics, and possesses the dual properties of a Bingham fluid and movement obstruction [1]-[4]. China, the United States, Switzerland, Colombia, and other countries are high-risk areas for debris flows. Regions prone to debris flows typically feature steep terrain, concentrated rainfall, and complex geological structures. These factors collectively make such regions high-risk zones for debris flows, which not only threaten the safety of local residents but also severely impact local economic development and social stability [5]-[8].

The occurrence and development of debris flows are influenced by various factors, such as geological structure, climate conditions, vegetation coverage, and land use patterns. In recent years, due to the intensification of global climate change and the impact of geological structural changes, the frequency and intensity of debris flows have both increased. The rise in extreme weather events has led to more frequent heavy rainfall, directly increasing the risk of debris flow occurrence [9]-[11]. Additionally, human activities have disrupted the natural environment, reduced vegetation coverage, and altered land use patterns, further increasing the probability of mudslides [12]-[13]. Since the movement and deposition characteristics of debris flows directly determine their destructive power and impact range, but debris flows often erupt suddenly, move at high speeds, have strong carrying capacity, and possess immense energy and destructive power, they also exhibit characteristics such as direct progression, intermittent flow, non-stationarity, unevenness, and erosiveness during their movement process [14]-[17]. This poses challenges for debris flow disaster rescue and forecasting efforts. Therefore, studying the movement and deposition process of debris flows through numerical simulation is of great importance and has strong practical

application value.

Shen et al. [18] designed a comprehensive numerical model for debris flows, which can simulate the entire process of debris flow outbreak, transport, entrainment, deposition, and property changes, with the outbreak mechanism being slope collapse and surface erosion. Long et al. [19] used a particle flow model and drift flux model to numerically simulate the material transport process of glacial debris flows, and introduced a fluid-solid coupling model to calculate the deposition characteristics of debris flows, effectively simulating the material transport process of glacial debris flows in high-altitude regions. Wang et al. [20] employed a combined approach of fluid-solid coupling models, moving object collision models, and renormalization group turbulence models to simulate the movement and deposition characteristics of boulders in a landslide at a specific location. The latter two models represent the landslide as a viscous fluid and the moving boulders as rigid bodies. dos Santos Corrêa et al. [21] proposed a numerical model for debris flows—rapid large-scale motion simulation—which simulates debris flow processes using Wallumi rheology and noted that debris flow processes in a certain region exhibit distinct granular characteristics. Lee et al. [22] combined the Wallumi equation and the shallow water equation to construct a two-dimensional debris flow model to simulate debris flow erosion, entrainment, and deposition processes. Abraham et al. [23] developed a two-dimensional numerical model for debris flow simulation, which incorporates three rheological models and interface operation functions. This model can predict debris flow flow parameters under spatiotemporal variations and perform parameter calibration through inverse analysis, thereby achieving dynamic simulation of debris flows. Hu et al. [24] employed the RNG k-c turbulence model and the bed material entrainment model to simulate debris flow motion and the bed material entrainment effects during motion, respectively. These materials undergo three stages: fragmentation, entrainment, and deposition. Topographic conditions and mechanical parameters are critical factors influencing the entrainment effects. Lee et al. [25] used the DAN3D model to simulate debris flow motion processes. This model exhibits high adaptability for numerical simulations of debris flows with extremely high flow velocities; however, its performance in estimating initial volume, gas flow growth rates, and rheological parameters is suboptimal. Cheng et al. [26] conducted a numerical analysis of debris flow erosion processes in earthquake-affected areas based on a deep average two-phase model. Vagnon et al. [27] used the RASH3D code based on continuum mechanics to numerically simulate debris flow movement in a basin and estimated its erodible depth by integrating a digital terrain model. Shu et al. [28] optimized the smooth particle hydrodynamics method and considered three interface force models—viscous forces, drag forces, and virtual mass forces—to simulate the formation process of a dam breach debris flow, with the generalized virtual mass force model contributing the most realistic simulation. Han et al. [29] integrated the Herschel-Burke-Papastathiou model, SPF, and the Bingham rheological model for numerical simulation of debris flow processes, with the simulation scheme considering the constitutive relationships between particles. In the aforementioned simulation models, there is insufficient analysis of the associated effects of plant debris, and the phase transition process has not been quantitatively described. Additionally, due to the large number of particles in the simulation process, computational efficiency is low, and parameter estimates may be biased, leading to prominent numerical simulation issues.

The dynamic characteristics of debris flows are influenced by various factors, such as the volume fraction of solid particles, particle size distribution, and the content of viscous materials [30], [31]. Erosion and deposition develop and change throughout the entire process of debris flow movement, leading to changes in the material composition ratio of the debris flow and further causing changes in the internal stress structure [32]-[34]. Different types of stress exhibit a complementary relationship within debris flows. When particle collision stress dominates, viscous stress decreases, as in water-stone flows, and vice versa [35]-[37]. Debris flow dynamics mathematical models should be established based on the material composition and internal stress characteristics of debris flows. Particle flow theory simulates the motion and interactions between regular particle media using the discrete element method, which is applicable to problems involving large deformations in solid mechanics [38]. Kang and Chan [39] conducted a two-dimensional particle flow entrainment numerical simulation experiment based on the discrete element method, which can calculate entrainment phenomena in particle flows, as well as the associated stresses and erosion depths, and is applicable to particle flow analysis. Albaba et al. [40] developed three elastic-plastic adhesive particle contact models supported by the discrete element method for numerical simulation of the formation process of mountainous debris flows. Particle flow not only characterizes the physical properties of macroscopic materials but also reflects microstructural characteristics that cannot be achieved by other methods [41].

Research has introduced an extended SPH method to simulate the interaction between slurry and dynamic objects during the movement and deposition of debris flows. Objects in the debris flow movement scene are treated as rigid bodies, and surface particle sampling is performed on the rigid bodies represented by triangular grids according to the Gaussian integration rule. A unified SPH method is used for force analysis of fluid particles and

surface particles. When handling the interaction between the slurry and static objects, collision detection algorithms are employed to screen surface particles in the slurry, thereby improving the efficiency of collision detection. The HBP constitutive model is integrated into the three-dimensional Navier-Stokes equation framework in SPH format for numerical simulation, yielding velocity field distributions and particle distributions in the longitudinal, transverse, and depth directions of the slurry, thereby investigating the rationality of the debris flow fluid model. Finally, based on the SPH numerical method, a three-dimensional debris flow numerical model of the Xiahegou watershed was constructed to simulate the movement process of debris flows in the channel and analyze the dynamic characteristics and deposition range of debris flows in Xiahegou.

II. Numerical simulation based on particle flow theory

II. A. Commonly used rheological models for debris flows

II. A. 1) Newtonian fluid model

Under laminar flow conditions, the rheological characteristics of clear water and low-concentration sandy water can generally be described using the Newtonian fluid model [42]. When a Newtonian fluid is subjected to shear flow, the relationship between shear stress and shear rate is as follows:

$$\tau = \mu_m \dot{\gamma} \tag{1}$$

Among them, μ_m is the dynamic viscosity coefficient, m²/s, and $\dot{\gamma}$ is the shear rate.

II. A. 2) Bingham fluid model

The Bingham fluid model describes the behavior of a fluid under shear stress. When the shear stress $\tau \le \tau_B$, the fluid does not flow. That is, the shear rate $\dot{\gamma}$ is zero. When $\tau > \tau_B$, the fluid flows, and its shear rate is linearly related to the shear stress, i.e.:

$$\tau = \tau_B + \eta \dot{\gamma} \tag{2}$$

In the equation, τ_B is the Bingham yield stress, Pa; η is the viscosity coefficient, Pa·s. The viscosity coefficient η is equivalent to μ_m in the previous formula.

When the yield stress $\tau_B > 0.5$ N/m², the sediment slurry is considered a Bingham fluid. The flocculation structure of the sediment slurry is related to the particle size distribution of the sediment particles, and the limiting concentration C_{vm} of the sediment particles reflects the particle size distribution of the sediment. According to relevant research, the relationship between the critical yield stress concentration C_{v0} and the maximum sediment concentration C_{vm} is:

$$C_{v0} = 1.26 C_{vm}^{3.2} \tag{3}$$

The relationship between the maximum sediment concentration C_{vm} and the sediment grain size distribution composition $\sum \Delta P_i d_i$ is as follows:

$$C_{vm} = 0.92 - 0.2 log \sum \Delta p_i / d_i \tag{4}$$

Among them, Δp_i is the weight percentage occupied by sediment particles with a grain size of d_i (mm).

II. A. 3) Power Law Model

(1) Power law model with yield stress

The power law model with yield stress can be regarded as a generalized expression of the sandy water body model, which is expressed as:

$$\tau = \tau_B + m \dot{\gamma}^n \tag{5}$$

In the equation, m is the fluid viscosity index. The higher the value of m, the greater the fluid's viscosity. τ_B, m, and n are collectively referred to as fluid rheological parameters. When $n \ne 1$, the fluid's shear rate is nonlinearly proportional to the shear stress; when n < 1, the fluid is a pseudoplastic material with yield stress, and when n > 1,

it is an expansive material with yield stress.

Considering the viscous, plastic, and collision effects in mudflow fluids, a general viscoplastic fluid model is proposed. The yield stress τ_B in the model is related to the fluid dynamic pressure p, the fluid cohesion c, and the friction angle φ, with the following relationship:

$$\tau_B = c\cos\varphi + p\sin\varphi \tag{6}$$

Among them, the fluid dynamic pressure p is related to the shear rate $\dot{\gamma}$ and the normal shear stress σ.

(2) Power law model

When $\tau_B = 0$, equation (5) becomes the power law model without yield stress:

$$\tau = m\dot{\gamma}^n \tag{7}$$

When $n \neq 1$, the fluid shear rate is linearly proportional to the shear stress. When $n < 1$, it is a plastic fluid model; when $n > 1$, it is an expansive fluid model.

(3) Collision model

When $\tau_B = 0$ and n=2, and the viscosity index m in equation (5) is replaced by α, it becomes the collision model:

$$\tau = \alpha\dot{\gamma}^2 \tag{8}$$

II. A. 4) Binomial Model

The binomial model is a model that simultaneously considers viscosity, plasticity, turbulence, and collisions. The relationship is as follows:

$$\tau = \tau_B + \mu_d \frac{du}{dy} + (\mu_c + \mu_1)(\frac{du}{dy})^2 \tag{9}$$

In the equation, μ_d is the dynamic viscosity coefficient, m²/s, and μ_c is the dispersion coefficient, which is proportional to the square of the particle size d and the square of the linear concentration λ. The relationship is given by: $\mu_c = \alpha_1 \rho_s \lambda^2 d^2$, where α_1 is an empirical coefficient, μ_i is the turbulence coefficient, $\mu_i = \rho_m l_m^2$, and l_m is the mixing length of the mixture.

II. B.SPH Algorithm

II. B. 1) Mathematical Principles

Before formally introducing the SPH algorithm, we will first introduce the basic concepts related to the SPH algorithm [43]:

(1) Definition of vector fields and scalar fields

Here, let there be an arbitrary point W in space. For W in space, there is a corresponding f(W), and f(W) is a directionless scalar. At this point, a scalar field is defined in this space. Similarly, for any point N in space, there is a corresponding vector f(N). Then, a vector field is defined in the space where W exists.

(2) Partial Derivative Formula

For a multivariate function $z = f(x, y)$, the partial derivative of z with respect to x at (x_0, y_0) is defined as:

$$\frac{\partial z}{\partial x} = \lim_{\Delta x \to 0} \frac{f(x_0 + \Delta x, y_0) - f(x_0, y_0)}{\Delta x} \tag{10}$$

(3) Hamilton operator

The Hamilton operator ∇ is very important in fluid mechanics. In general, this symbol is used as a symbol of fluid mechanics. An “operator” is a mathematical symbol that must be used in conjunction with other symbols and cannot exist independently. It is equivalent to “d” in mathematical differentiation. The Hamilton operator is defined as follows:

$$\nabla = \vec{x}\frac{\partial}{\partial x} + \vec{y}\frac{\partial}{\partial y} + \vec{z}\frac{\partial}{\partial z} \tag{11}$$

Although the Hamiltonian operator itself is not a vector scalar, many operations treat it as a vector. For example,

applying the Hamiltonian operator to a scalar field $A = f(x, y, z)$ yields:

$$\nabla A = \vec{x}\frac{\partial f}{\partial x} + \vec{y}\frac{\partial f}{\partial y} + \vec{z}\frac{\partial f}{\partial z} \tag{12}$$

In the above equation, A is a scalar, and the Hamiltonian operator is a vector. The product of a vector and a scalar is a vector. When the Hamiltonian operator is applied to the vector field A, it can be seen from the following equation that the operation of the Hamiltonian operator on the vector field can be regarded as the dot product of vectors, and the result is a scalar:

$$\nabla \cdot \vec{A} = (\vec{x}\frac{\partial}{\partial x} + \vec{y}\frac{\partial}{\partial y} + \vec{z}\frac{\partial}{\partial z}) \cdot (\vec{x}A_x + \vec{y}A_y + \vec{z}A_z) = \frac{\partial A_x}{\partial x} + \frac{\partial A_y}{\partial y} + \frac{\partial A_z}{\partial z} \tag{13}$$

Divergence describes the degree of dispersion of a vector field.

II. B. 2) Formulas related to the SPH algorithm

SPH stands for Smooth Particle Hydrodynamics, a method whose core idea is to discretize fluid motion into the motion of particles that exert forces on each other. The relevant physical properties of each particle are obtained by superimposing the relevant properties of the surrounding particles. Each individual particle follows Newton's second law:

$$m\vec{a} = \vec{F} \tag{14}$$

In SPH, the density of fluid cells determines fluid mass, so mass is usually replaced by density:

$$\rho\vec{a} = \vec{F} \tag{15}$$

The force acting on a particle consists of three components, as shown in Figure 1.

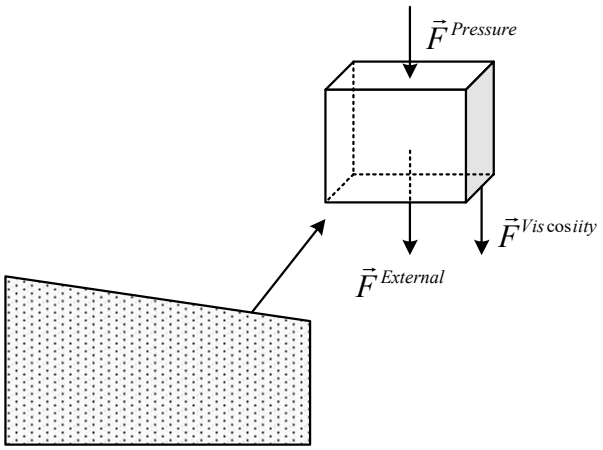

Figure 1: Schematic diagram of force acting on a particle

As can be seen from the figure, a particle is subject to forces in three directions, where $\vec{F}External$ is the gravitational force acting on the particle:

$$\vec{F}External = \rho\vec{g} \tag{16}$$

In the above equation, $\vec{F}pressu$ is the pressure generated between particles within the fluid. Its numerical value is equal to the gradient of the pressure field, and its direction points toward the low-pressure region:

$$\vec{F}pressure = -\nabla p \tag{17}$$

During particle flow, viscous forces $\vec{F}Vis\cos ity$ are generated. Imagine that within a flowing liquid, the force exerted by the faster-moving parts on the slower-moving parts is equivalent to shear force. The viscosity coefficient

of the fluid and the velocity difference affect the magnitude of this force:

$$\vec{F}Viscpsity = \mu\nabla^2\vec{u} \tag{18}$$

The resultant force acting on the particle can be obtained from the above equation:

$$\rho\vec{a} = \rho g - \nabla p + \mu\nabla^2\vec{u} \tag{19}$$

The above formula is essentially a simplified form of the N-S equation. Similar to other mathematical methods in fluid mechanics, the SPH algorithm also incorporates the concept of a “smooth kernel.”

Suppose there is a point r in the fluid, where there may not necessarily be particles. Within the particle influence range, i.e., the smooth kernel radius h, there are j particles with positions $r_0, r_1, r_2, \cdots, r_j$ respectively. Then, the accumulation formula for a certain property A at this point is:

$$A(\vec{r}) = \sum_j A_j \frac{m_j}{\rho_j} w(\vec{r} - \vec{r}_j, h) \tag{20}$$

In the above equation, A represents a certain particle property to be accumulated in the debris flow particles (solid or liquid particles). m_j and p_j represent the mass and density of the particles surrounding r. r_j is the spatial position of one of the surrounding particles, including the X, Y, and Z coordinates, and h is the influence range of the particle, i.e., the smooth kernel radius. The function w is the smoothing kernel function, which has two important properties: first, the smoothing kernel function must be an even function; second, the smoothing kernel function is a regular function, i.e., $\int W(r)dr = 1$. The derivation formula for the acceleration $a(r_i)$ at the spatial position r_i is:

$$\vec{a}(r_i) = \vec{g} - \frac{\nabla p(r_i)}{\rho(r_i)} + \frac{\mu\nabla^2\vec{u}(r_i)}{\rho(r_i)} \tag{21}$$

To determine the net force acting on particle i, it is necessary to derive the density, pressure, velocity, and related cumulative functions for particle i individually, which yields the following equation:

$$\rho(\vec{r}_i) = \sum_j \rho \frac{m_j}{\rho} W(\vec{r}_i - \vec{r}_j, h) \tag{22}$$

When calculating the density at position r_i, a smoothing kernel function is used. This smoothing kernel function is called the Poly6 function, and its specific form is shown below:

$$W_{pol6}(\vec{r}, h) = K_{pol6}(h^2 - r^2)^3, 0 \le r \le h \tag{23}$$

K_{poly6} is a fixed coefficient. By integrating and combining the regularization properties of the smoothing kernel function, if the simulation environment is 2D, its value can be obtained by integrating in polar coordinates:

$$K_{pol6} = 1/\int_0^{2\pi}\int_0^h r(h^2 - r^2)^3 drd\theta = \frac{4}{\pi h^8} \tag{24}$$

If the simulated environment is 3D, calculating the integral in spherical coordinates yields the value of K_{poly6} as:

$$Kpoly6 = 1/\int_0^{2\pi}\int_0^{\pi}\int_0^h r(h2 - r2)3drd\varphi d\theta = \frac{315}{64\pi h^9} \tag{25}$$

Since the SPH algorithm treats all particles in the fluid as having the same mass, the density calculation formula at r_i in a 3D environment is as follows:

$$\rho(ri) = m\frac{315}{64\pi h^9}\sum_j (h^2 - |\vec{r}_i - \vec{r}_j|^2)^3 \tag{26}$$

Based on the above equation, the pressure calculation formula at position r_i can be derived:

$$\vec{F}i^{pressure} = -\nabla p(\vec{r}_i) = -\sum_i p_j \frac{m_j}{\rho_i} \nabla W(\vec{r}_i - \vec{r}_j, h) \tag{27}$$

The force between two particles located in different pressure regions in a fluid is different, and the pressure is not balanced. Therefore, in calculations, the average pressure of the two particles is usually used to calculate the pressure exerted on a single particle:

$$\vec{F}_i^{pressure} = -\sum_j \frac{m_j (p_i + p_j)}{2\rho_j} \nabla W(\vec{r}_i - \vec{r}_j, h) \tag{28}$$

The ideal gas equation can be used to calculate the pressure P generated by a single particle:

$$p = k(\rho - \rho_0) \tag{29}$$

In the above equation, ρ is the static density of the liquid phase of the debris flow, and k is a temperature-dependent fluid-related constant. The smooth kernel function used in pressure calculations is called the Spiky function:

$$W_{spik}(\vec{r}, h) = K_{spik}(h - r)^3, 0 \le r \le h \tag{30}$$

In 3D, $Kspiky = 15/(\pi^* h^6)$. That is:

$$\nabla W_{spiky}(\vec{r}, h) = \nabla \frac{15}{\pi h^6}(h - r)^3 = -\vec{r}\frac{45}{\pi h^6 r}(h - r)^2 \tag{31}$$

According to the above formula, the acceleration generated by the pressure between particles can be calculated as follows:

$$\vec{a}_i pressure = -\frac{\nabla p(\vec{r}_i)}{\rho i} = m\frac{45}{\pi h 6}\sum_j (\frac{pi + pj}{2\rho i \rho j}(h - r)2\frac{\vec{r}_i - \vec{r}_j}{r}) \tag{32}$$

From the last part of equation (32), we can see that the effect caused by viscosity is as follows:

$$\vec{F}_i^{viscosity} = \mu\nabla^2 \vec{\mu}(\vec{r}_i) = \mu\sum_j \vec{u}_j \frac{m_j}{\rho_j} \nabla^2 W(\vec{r}_i - \vec{r}_j, h) \tag{33}$$

When calculating the viscous force between particles in a debris flow, there is also an issue of imbalance. The velocity in the formula is not the absolute velocity but the average velocity between particles. Therefore, the correct formula for calculating the viscous force is:

$$\vec{F}_i^{viscoity} = \mu\sum_j m_j \frac{\vec{u}_j - \vec{u}_i}{\rho_j} \nabla^2 W(\vec{r}_i - \vec{r}_j, h) \tag{34}$$

The form of the smooth kernel function is as follows:

$$W_{viscosity}(\vec{r}, h) = K_{viscosity}(-\frac{r^3}{2h^3} + \frac{r^2}{h^2} + \frac{h}{2r} - 1), 0 \le r \le h \tag{35}$$

$$Kvis\cos ity = 15/(2 * \pi * h^3) \tag{36}$$

$$\nabla^2 W_{viscosity}(\vec{r}, h) = \nabla^2 \frac{15}{2\pi h^3}(-\frac{r^3}{2h^3} + \frac{r^2}{h^2} + \frac{h}{2r} - 1) = \frac{45}{\pi h^6}(h - r) \tag{37}$$

The resulting acceleration is:

$$\vec{a}_i vis\cos ity = \frac{\vec{F}_i vis\cos ity}{\rho_i} = m\mu\frac{45}{\pi h^6}\sum_j \frac{\vec{\mu}_j - \vec{\mu}_i}{\rho_i\rho_j}(h-|\vec{r}_i - \vec{r}_j|) \tag{38}$$

Combining all of the above equations, the acceleration of particle i can be obtained from the following formula:

$$\begin{aligned}\vec{a}_i(\vec{r}_i) = \vec{g} + m\frac{45}{\pi h^6}\sum_j (\frac{p_i + p_j}{2\rho_i\rho_j}(h-r)^2\frac{\vec{r}_i - \vec{r}_j}{r}) \\ +m\mu\frac{45}{\pi h^6}\sum_j \frac{\vec{\mu}_j - \vec{\mu}_i}{\rho_i\rho_j}(h-r)\end{aligned} \tag{39}$$

II. C.Solid particle motion equation

The movement and deposition process of debris flows primarily depends on the solid particles within them. Previous researchers have focused on the movement of solid particles in debris flows. This paper treats debris flows as two-phase flows (liquid and solid), simulates their movement and deposition, and calculates and analyzes the interaction results along their path. Subsequently, the resultant force is calculated using the SPH algorithm, and the real-time position of the particles is determined using the Navier-Stokes equations. Based on rigid body kinematics, the motion equation for solid sediments can be expressed as:

$$V_S = V_{S\_P} + \omega \times r \tag{40}$$

In the above equation, VS represents the velocity of solid particles in the solid phase of a debris flow, VS_P represents the average velocity of solid particles, and ω represents the instantaneous angular velocity of solid particles.

During the motion of solid particles, in addition to translational motion, rotational forces also exist. If rotational forces are neglected, the simulated debris flow motion will appear very rigid. Assuming the rotational inertia of the solid is I and the angular momentum is L, the angular velocity of its rotation is as follows:

$$\omega = I^{-1}L \tag{41}$$

In order to reduce the amount of calculations and improve efficiency, this paper only considers the translational motion of rigid particles. The core idea of using SPH to solve the N-S equations is to calculate the resultant force acting on a particle based on the resultant force it experiences (Newton's second law). Once the resultant force is calculated, the real-time position of the particle can be obtained.

III. Modeling of debris flow movement and accumulation processes

III. A. Modeling of Mudslide Movement

III. A. 1) Interaction between slurry particles and static objects

When the liquid phase slurry and solid phase objects of a mudslide interact, the interaction is achieved through the interface formed by their contact. Since the boundary is always stationary, to reduce the amount of calculation, the interaction between the slurry and the static object is treated as a one-way coupled motion. When a collision occurs, the reaction force exerted by the static object on the fluid particles is calculated.

III. A. 2) Interaction between liquid slurry and dynamic objects

This section models slurry and solids based on the SPH method. The algorithm implementation process is described as follows:

(1) Read the position information of liquid phase slurry particles and rigid body surface sampling particles.
(2) Initialize the physical properties of the particles, such as density, velocity, and position.
(3) Query the neighboring particles around the slurry particles.
(4) Calculate the density and pressure of the slurry particles.
(5) Calculate the internal and external forces acting on the slurry particles.
(6) For the solid surface sampling particles, query the surrounding slurry particles.
(7) Solve for the forces exerted by the slurry particles on the solid particles.
(8) Update the position and velocity of slurry particles using the frog leap algorithm.
(9) Calculate the net force acting on the solid based on the forces acting on particles on the solid surface, and update the motion state of the solid.

(10) Repeat steps (3)-(9).

The process of solving the interaction between liquid slurry and solid objects using the SPH algorithm is shown in Figure 2.

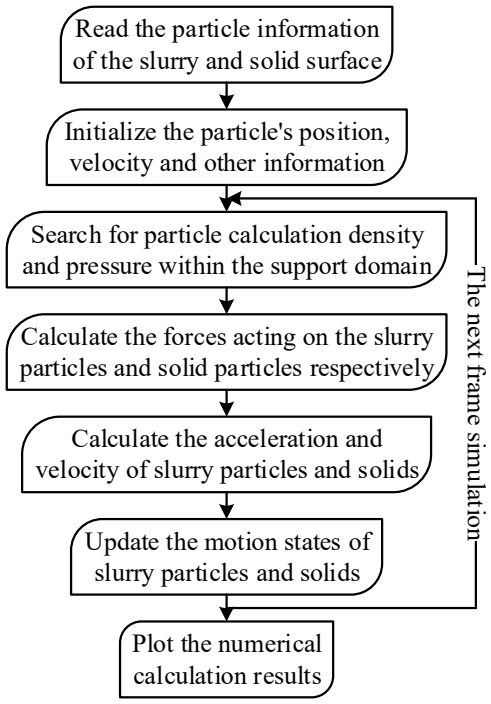

Figure 2: Flowchart of fluid-structure coupling algorithm based on SPH method

III. B. Particle Force Analysis and State Update

III. B. 1) Force analysis and state update of liquid phase slurry particles

Updating the position, velocity, and other motion states of liquid phase slurry particles is key to simulating debris flow motion. Since the SPH method is a Lagrangian method, that is:

$$\rho \frac{Du}{Dt} = -\nabla p + \mu \nabla^2 u + \rho g \tag{42}$$

In this equation, ρ represents the density of the slurry particles, u represents the velocity of the slurry particles, p represents the pressure exerted on the slurry particles, g represents the gravitational acceleration, and μ represents the viscosity coefficient of the particles.

To ensure that the fluidized boundary is not penetrated and to partially address the issue of underestimated particle density at the boundary, the boundary particles are included in the density calculation formula for the fluid particles, i.e.:

$$\rho_{f_i} = \sum_j m_{f_j} W_{ij} + \sum_k m_{b_k} W_{ik} \tag{43}$$

where f_j denotes boundary particle j, b_k denotes boundary particle k, the first summation is performed over all fluid neighbor particles of fluid particle i, and the second summation is performed over all particles sampled from the contacting solid surfaces.

If the summation on the right-hand side of equation (43) is regarded as the resultant force acting on slurry particle i, then equation (43) is equivalent to Newton's second law, i.e., equation (44):

$$a_i = \frac{Du_i}{Dt} = \frac{f_i}{\rho_i} \tag{44}$$

where a_i represents the acceleration of particle i, f_i represents the net force acting on particle i, and ρ_i represents the density of particle i.

The SPH method is used to discretize the motion of the liquid phase of a debris flow into a series of particles, and the flow of the debris is simulated by updating the motion states of these particles. That is:

$$a_i = \frac{f_{FF} + f_{RF} + f_{external}}{\rho_i} = (f_i^{pressure} + f_i^{viscosity} + \rho_i g + f_i^{collision} + f_i^{surface}) / \rho_i \tag{45}$$

In the equation, f_{FF}, f_{FR} represent the forces exerted on slurry particle i by other slurry particles and surrounding solid particles, respectively, while $f_{extermal}$ denotes the net external force acting on the slurry particle. $f_i^{pressure}, f_i^{viscosity}, f_i^{collision}, f_i^{surface}$ respectively represent the total pressure, viscous force, collision force, and surface tension acting on the slurry particle:

$$f_i^{itpressure} = f_{FF}^{itpressure} + f_{RF}^{itpressure} \tag{46}$$

This paper uses an improved pressure calculation formula:

$$f_i^{pressure} = -\sum_{j \neq i} (\frac{P_i + P_j}{2\rho_j}) m_j \nabla W(r_i - r_j, h) \tag{47}$$

Based on the stress analysis, it can be further broken down into the following equations:

$$\begin{aligned} f_i^{pressure} &= \sum_{j=1}^{N} m_{Rj} \frac{(p_i + p_j)}{2\rho_i} \nabla W(x_i - x_j, h_F) \\ &+ \sum_{j=1}^{N} m_{Fj} \frac{(p_i + p_j)}{2\rho_i} \nabla W(x_i - x_j, h_R) \end{aligned} \tag{48}$$

The viscous forces acting on liquid-phase slurry particles originate from both fluid particles and rigid particles, as shown in equation (49):

$$f_i^{viscocity} = f_{FF}^{viscocity} + f_{FR}^{viscocity} \tag{49}$$

Using the viscous forces $f_{FF}^{viscocity}, f_{RF}^{viscocity}$ acting on the slurry particles, the total viscous force acting on the particles is obtained according to formula (50):

$$\begin{aligned} f_i^{viscocity} &= \mu_F \sum_{j=1}^{N} m_{Fj} \frac{(u_j - u_i)}{\rho_i} \nabla^2 W(x_i - x_j, h_F) \\ &+ \mu_R \sum_{j=1}^{N} m_{Rj} \frac{(u_j - u_i)}{\rho_i} \nabla^2 W(x_i - x_j, h_R) \end{aligned} \tag{50}$$

To simplify the calculation, this paper assumes that the collision between the slurry particles and the object is an ideal collision with no energy loss. According to the law of conservation of momentum:

$$f_i^{collision} = \sum_{j=1}^{N} m_{Fj} \frac{(\upsilon_t - \upsilon_0)}{t} + \sum_{j=1}^{N} m_{Rj} \frac{(\upsilon_t - \upsilon_0)}{t} \tag{51}$$

In the equation, m_f, h_F, m_R, h_R represent the mass of the slurry particles, the smooth kernel radius of the slurry particles, the mass of the solid particles, and the smooth kernel radius of the solid particles, respectively. ρ is the density of the fluid particles.

The external force is calculated using equation (52), and the surface tension is calculated using equation (53):

$$f_i^{gravity} = \rho_i g \tag{52}$$

$$f_i^{surfice} = \begin{cases} -\sigma \dfrac{n_i \sum \dfrac{m_j}{\rho_j} \nabla^2 W(r_i - r_j, h)}{\| n_i \|}, & \| n_i \| \geq l \\ 0 & \text{other} \end{cases} \tag{53}$$

where n_i is the normal vector of the slurry surface, obtained using formula (54):

$$n_i = \sum \frac{m_j}{\rho_j} \nabla W(r_i - r_j, h) \tag{54}$$

III. B. 2) Analysis of forces acting on solid particles

The solid-phase particle is subjected to forces from the slurry particles, denoted as f_{FR}, forces from the solid-phase object, denoted as f_{RR}, and external forces, denoted as $f_{external}$. The resultant force acting on the solid-phase particle is calculated using equation (55):

$$f_R = f_{FR} + f_{RR} + f_{external} \tag{55}$$

To solve for the pressure exerted on solid particles using the SPH method, we first need to solve for the pressure at the particle's location using formula (56):

$$p_i = \sum p_j \frac{m_j}{\rho_j} W(r_i - r_j, h) \tag{56}$$

According to the relationship between pressure and pressure, use formula (57) to solve for the pressure exerted on the particle:

$$f_i^{pressure} = -p_i S_i \frac{\vec{n}_i}{\| n_i \|} = -p_i \pi R_i^2 \frac{\vec{n}_i}{\| n_i \|} \tag{57}$$

In the equation, S_i represents the area, R_i represents the radius of particle i, and $\vec{n}_i$ is the surface normal vector.

After calculating the resultant force acting on the solid particles, the resultant force acting on the particles is weighted and summed according to the Gauss integration rule, ultimately yielding the resultant force acting on the solid object. The resultant torque is then calculated using formula (58):

$$\tau = (r - r^g) \times F \tag{58}$$

Among them, r^g is the position of the center of mass of the particle to which the particle belongs.

III. B. 3) Solid Phase Object State Update

When using the motion of solid surface particles to represent the motion of rigid bodies, the total mass of the solid is calculated using formula (59):

$$M = \sum_j m_j \tag{59}$$

In the equation, M represents the total mass of the solid, and m_j represents the mass of a surface particle.

Assuming that all particles on the solid surface have the same mass, the velocity of the center of mass is calculated using equation (60). In the equation, N represents the total number of sampled particles on the solid surface, and v_j represents the velocity of a single sampled particle j on the solid surface. That is:

$$v_g = \frac{1}{N} \sum_j v_j \tag{60}$$

The angular velocity of the solid's center of mass rotation can be calculated using equation (61). The solid's

moment of inertia I can be solved using formula (62). In the formula, q_j represents the position of a single surface sampling particle j. That is:

$$\omega = \frac{1}{I}\sum_j q_j \times v_j \tag{61}$$

$$I = \sum_j |q_j|^2 \tag{62}$$

Using the above formulas to calculate the center of mass velocity and angular velocity of the solid, the velocity of each sampled particle on the solid surface can be calculated using formula (63):

$$v_j = v_g + \omega \times q_j \tag{63}$$

The motion of a solid is represented by the motion of its center of mass, so it is necessary to find the position of the center of mass. The position of the center of mass r_g is the sum of all surface particles, that is:

$$r_g = \frac{1}{N}\sum_j r_j \tag{64}$$

In the simulation process, to ensure that the shape of the solid does not change, it is necessary to ensure that the position of the relative center of mass of the surface sampling particles remains constant. The relative position q_j is solved using formula (65):

$$q_j = r_j - r_g \tag{65}$$

When using the SPH method to simulate solid motion, it is necessary to update the position of each solid particle through the rotation matrix $R(t)$. The center of mass matrix and rotation matrix are calculated using formula (66):

$$\begin{cases} r_g(t+\Delta t) = r_g(t) + \Delta t v_g(t+\frac{1}{2}\Delta t) \\ R(t+\Delta t) = R(t) + \Delta t Q(t+\frac{1}{2}\Delta t) \end{cases} \tag{66}$$

In the equation, $Q(t)$ represents the rate of change of the rotation matrix, which is calculated using formula (67). That is:

$$Q(t) = \begin{vmatrix} 0 & -\omega_z & \omega_y \\ \omega_z & 0 & -\omega_x \\ -\omega_y & \omega_x & 0 \end{vmatrix} R(t) \tag{67}$$

The overall position and transformation matrix of the solid are calculated according to formula (67). In order to keep the shape of the solid unchanged, the rotation matrix and relative position are used to update the position r_j of the solid surface particles, as shown in formula (68):

$$r_j(t+\Delta t) = R(t+\Delta t)(r_j(t) - r_g(t)) + r_g(t+\Delta t) \tag{68}$$

III. C. Collision Detection and Handling

III. C. 1) Collision Detection

The collision detection algorithm between fluid particles and triangular meshes is as follows:

Step 1: Calculate the normal vector $\vec{n}$ of the triangular mesh.

Step 2: Calculate the motion trajectory for the next time step based on the physical information carried by the particle.

Step 3: Determine whether the ray containing the fluid particle intersects with the plane containing the triangle.

III. C. 2) Motion processing of liquid slurry

Based on the speed after the collision, it can only reach point D. According to the principle of non-penetration, when the collision occurs, calculate the reaction force:

$$f = k^s dn + k^d (v * n)n \tag{69}$$

Where f is the reaction force exerted by the object during the collision, i.e., the external force term on the right-hand side of the N-S equation, k^s is the spring constant, and k^d is the damping constant. To achieve the desired effect, k^s and k^d can be adjusted according to actual conditions.

IV. Experimental verification

IV. A. Selection of constitutive models

To validate the rationality of the numerical model, this paper combines the results of mudslide dam failure experiments for verification. In the experiment, researchers altered the relative content of soil and water to obtain a series of mud mixtures with different volume concentrations C_v. Key physical properties such as density ρ, yield strength τ_y, and viscosity coefficient μ_B were measured. The mudflow dam failure experiment was conducted in a smooth water channel with a length of 5.0 m, width of 2.0 m, and a bottom slope of 0.1%. The tested mud mixture was initially placed in a 2.0 m long and 1.5 m wide space on the right side of the channel, with an initial height of 0.2 m, separated by a movable partition. At the start of the experiment, the movable partition was removed to allow the mud mixture to flow freely, and the deformation of the mud front and the distance traveled by the front were recorded at various time points.

To ensure the authenticity of the data, this paper selected the experimental group with the most comprehensive parameters and experimental results data from the above experimental studies, with a volume concentration C_v = 20.5%, for numerical simulation. The original experiment measured C_v = 20.5%, the density of the mud mixture was 1329 kg/m^3 based on the Bingham model. The yield stress and viscosity coefficient were obtained as 1.97 Pa and 0.025 Pa·s, respectively. The comparison of the fitting results between the Bingham model and the HBP model is shown in Figure 3. In the figure, the dots represent the experimental measured values, and the yellow dashed line represents the fitting results based on the Bingham model. The Bingham fitting results generally agree with the experimental values under large deformations, but when $\dot{\gamma}$ <33, there is a significant error between the fitting results and the experimental values, and when $\dot{\gamma}$ >125, the error between the fitting results and the experimental values gradually increases. In this paper, the HBP model is used for curve fitting adjustment. By changing the value of m to reduce the error of the fitted curve in the plastic-yield transition region, and by changing the value of n to reduce the error of the fitted curve under large deformation. The final values of m = 0.14 and n = 1.02 were determined, yielding the HBP fitting curve, shown as the orange solid line in the figure.

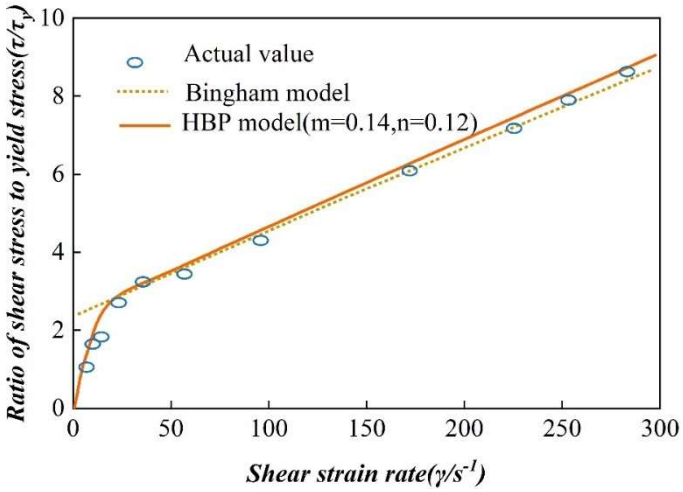

Figure 3: Comparison of the fitting results of Bingham model and HBP model

This study was modeled based on the actual three-dimensional dimensions of the experiment. The initial spacing between SPH fluid particles was set to dp = 0.0048 m, and the smoothing length was determined as

$h = (3(dp)^2)^{1/2}$, which is approximately 1.71 times the initial particle spacing. The initial time step was set to 1.0×10^{-4} s. The Courant-Friedrich-Lewy (CFL) number was set to CFL = 0.2, and the Verlet time integration algorithm was employed to simulate the fluid flow state over 1.000 s. The modeling results and key parameters are shown in Figure 4 and Table 1. Numerical simulations obtained the particle distribution and velocity field distribution at various time instants. The velocity field distribution at various time instants is shown in Figure 5, where Figure 5(a) shows the distribution of propagation velocity along the depth and longitudinal directions at the mid-section of the mud (Y = 0.066 m), and Figure 5(b) shows the lateral distribution of propagation velocity at the mud surface. The maximum propagation velocity occurs at the front end of the fluid and gradually decreases toward the rear end. As time progresses, the front-end velocity first increases, reaches a peak, and then gradually decreases. From the lateral velocity field distribution, due to the influence of boundary constraints, the velocity at the center of the same cross-section is higher than that at the sides, and the lateral distribution of the particles at the leading edge exhibits a symmetrical arc shape.

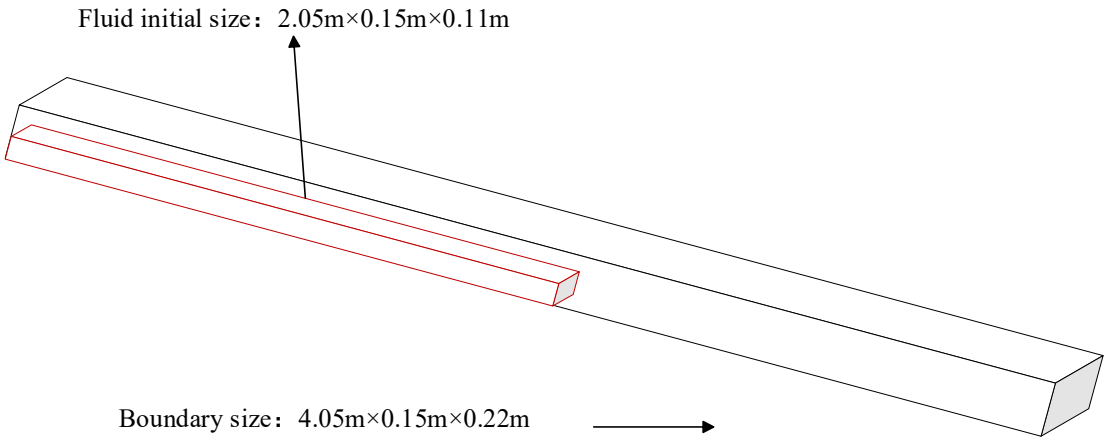

Figure 4: Geometry of simulation model

Table 1: Parameters used in the simulation

Parameter	Magnitude
Fluid density $\rho / (kg / m^3)$	1329
The viscosity coefficient $\mu_B / (Pa \cdot s)$	0.025
Yield strength $\tau_y / (Pa)$	1.97
Fluid particles number Npf	232500
The boundary particle number Npb	75225
Particle interval dp / m	0.0048
Analog time $t / (s)$	1.000
Smooth length h / m	0.0088
Time of step $\Delta t / s$	0.0001

This paper selects two instantaneous points, t=0.37s and t=0.60s, and compares the SPH numerical simulation results with the experimental results under different constitutive relationships based on the HBP, Cross, and Bingham constitutive models. The particle distribution along the longitudinal section (Y=0.066m) is shown in Figure 6. Additionally, this paper compares the temporal evolution of the mud front movement distance obtained from numerical simulations with the original experimental test results, as shown in Figure 7. Combining the two figures shows that the surface shapes of the mud longitudinal profiles obtained from numerical simulations under the three constitutive models generally agree with the experimental results. However, the particle distribution in the central region of the leading edge lags slightly behind the actual results, and the relationship between the leading edge movement distance and time growth is close to the experimental results. During the initial stage of mud movement, the results of the Cross model and Bingham model are similar and both lag behind the HBP model simulation results.

Subsequently, the simulation results of the three models gradually converge.

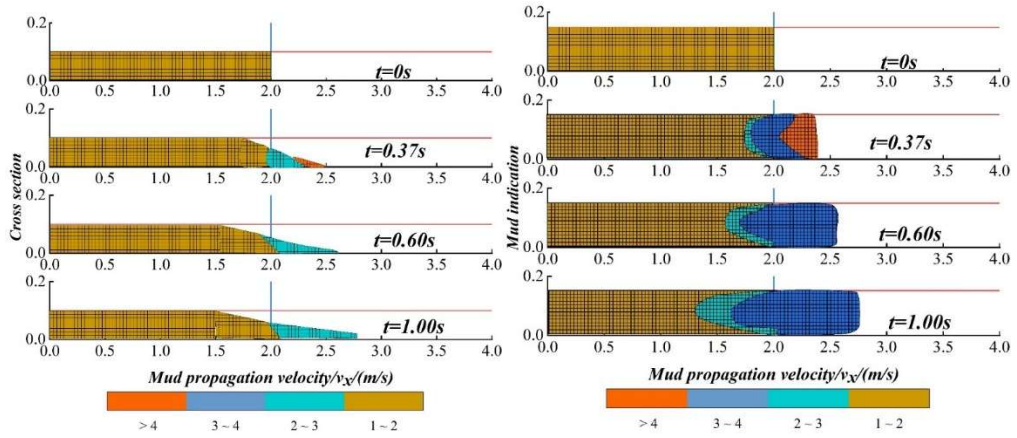

(a)Mud middle cross section (b) Mud surface

Figure 5: Velocity field of the simulation at different time

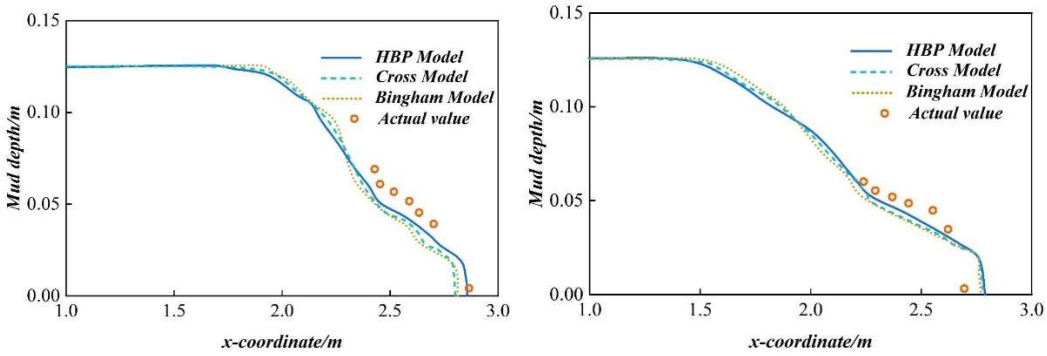

(a) t=0.37s

(b) t=0.60s

Figure 6: Surface profiles of mudflow after dam break at time t=0.37s and 0.6s

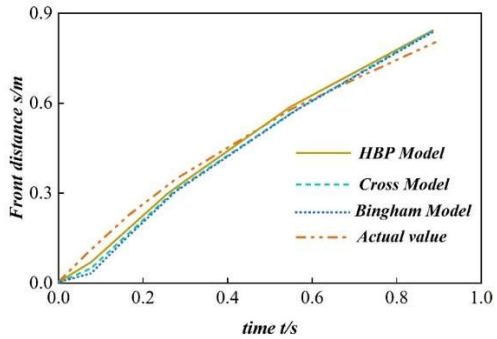

Figure 7: The distance of the mud is compared

When using the three-dimensional SPH method based on the HBP constitutive model to invert the experiment, the simulation results are basically consistent with the experimental results. Compared with the simulation results

of the Cross and Bingham models, the HBP simulation results in this paper are ahead of the former two in the early stage of mud movement and have better accuracy, and then gradually converge with the former two. This is because, within the plastic strain transition zone of the mud, the shear stress values obtained from the HBP model are generally lower than those from the Bingham model, resulting in the fluid exhibiting a more “dilute” rheological characteristic. At this stage, the fluid motion simulated by the HBP model is faster than that of the Bingham and Cross models. Subsequently, due to the influence of n (n=1.01>1), the HBP model exhibits a certain degree of shear thickening behavior in the large deformation stage, causing the fluid motion trend to lag relatively, ultimately leading the HBP model to gradually converge with the simulation results of the Cross and Bingham models. The above results also validate the rationality of the numerical model adopted in this study and further demonstrate the advantages of the HBP model in the detailed description of the rheological properties of debris flows.

IV. B. Analysis of the landslide process

IV. B. 1) Numerical simulation of the movement accumulation process

Based on the debris flow displacement map, at 125 steps, a small amount of particle movement occurs at the front of the debris pile. When reaching 2.5×10⁶ steps, a large amount of particle movement occurs, with some particles already sliding to the bottom of the gully. At 5.0×10⁶ steps, most particles have already slid to the bottom of the gully, and particle movement tends to stabilize, with the maximum particle displacement reaching approximately 22 m. The debris flow velocity displacement diagram shows that at 125 steps, the vector directions of most particles are downward, indicating that particles are accumulating downward under the influence of gravity. A small number of particles at the front of the debris pile have vector directions pointing forward, indicating that some particles have begun to slide. At 2.5×10⁶ steps, the vector directions of most particles point toward the gully bottom, and a small number of particles have reached the gully bottom. At 5.0×10⁶ steps, most particle vectors have reached the gully bottom, indicating that the sliding has stabilized.

Figure 8 shows the X-direction displacement changes of particles at monitoring points 1–3. It can be seen that monitoring point 1 is located at the lower part of the accumulation body. When sliding begins, the X-direction displacement increases rapidly, indicating that particles first slide out of the accumulation body at the start. At 1.2×10⁶, the velocity slowed down as particles reached the bottom of the gully. Monitoring point 2 is located in the middle of the debris pile, with displacement increasing uniformly, indicating that particles in this section remained in motion throughout the sliding process. Monitoring point 3 is located at the upper part of the debris pile, with its displacement distance significantly smaller than that of monitoring points 1 and 2.

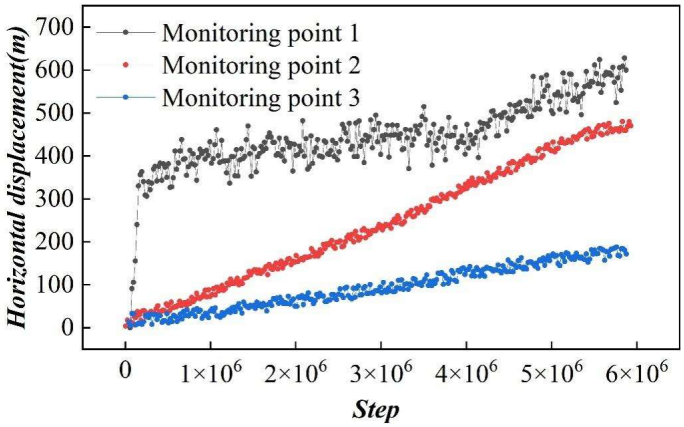

Figure 8: The deposit is monitored by the particle displacement curve

Figure 9 shows the changes in porosity at different locations within the pile. As can be seen from the figure, the measured circular porosity at different locations reaches 1 sequentially, indicating that particles within the measured circle exit the circle sequentially. Measured circle 1 is located at the lower part of the pile. Since all particles must exit before the porosity reaches 1, the time step is the longest. Measured circle 3 is located at the rear part of the pile, where the porosity reaches 1 after all particles have exited. Measured circle 2 is positioned between the two.

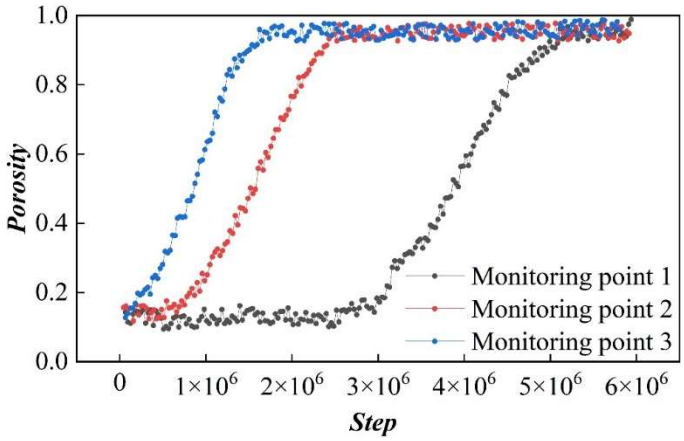

Figure 9: Different location porosity curve

In summary, the process of the accumulation body sliding downward can be inferred as follows: due to factors such as rainfall, the strength of the particles at the bottom of the accumulation body is reduced, causing them to slide downward. The particles at the top, having lost the support of the particles below, continue to slide downward, causing the entire accumulation body to slide and resulting in a mudslide disaster.

IV. B. 2) Effect of particles on convection velocity

(1) Fluid containing an overlying coarse-grained layer

Now, we apply the above equation to the observed array flow situation (a). The unit volume mass is 2000 kg, the initial flow velocity is v_0 = 1.6 m/s, assuming the thickness of the overlying coarse layer is h_1 = 0.28 m, and the thickness of the underlying layer is h_2 = 0.72 m. The basic calculation parameters for the debris flow are shown in Table 2.

Table 2: Debris flow calculation parameters

Parameter	$c(kPa)$	$\varphi(°)$	$\alpha(°)$	$G_r / G_r^{'}$	S_t	$e / e^{'}$
Value	0.09	2.55°	12°	2.77/2.73	0.88	0.41/0.35

Then, the relationships between "$v_1 - U_p$" and "$a_1 - U_p$" can be used for flow containing an overlying coarse-grained layer. The relationship between velocity and pore water pressure in fluids containing an overlying coarse-grained layer is shown in Figure 10, and the relationship between acceleration and pore water pressure is shown in Figure 11.

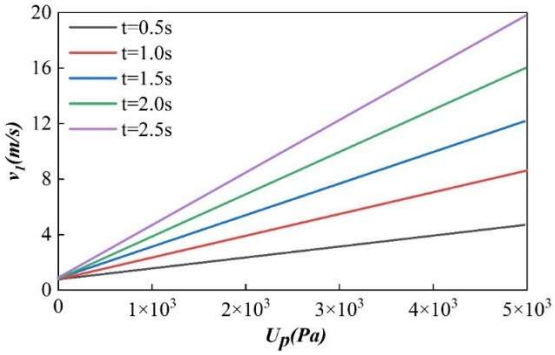

Figure 10: Relationship between velocity and pore water pressure in flow with overlying layer

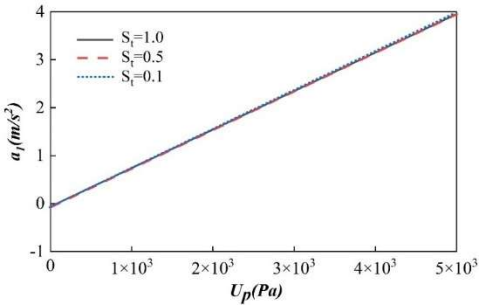

Figure 11: Relationship between acceleration and pore water pressure

It can be seen that velocity and acceleration are positively correlated with pore water pressure. In other words, under certain conditions during debris flow movement, the faster the rate of velocity increase, the greater the increase in pore water pressure. This is mainly because during movement, particles interlock and compress each other, narrowing the water transport channels, and the water stored in the space continuously undergoes dynamic loading, exacerbating the generation of excess pore water pressure.

(2) Uniformly mixed flow

For uniformly mixed debris flows, the relationship between $v_2 - U_p$ is shown in Figure 12, and the parameters are shown in Table 3.

Table 3: Calculating parameters

Parameter	$c(kPa)$	$\varphi(°)$	$\alpha(°)$	(μ, D_c)	$\rho_s(kg/m^3)$
Value	0.09	2.55°	12°	(0.055,14.88)	1822

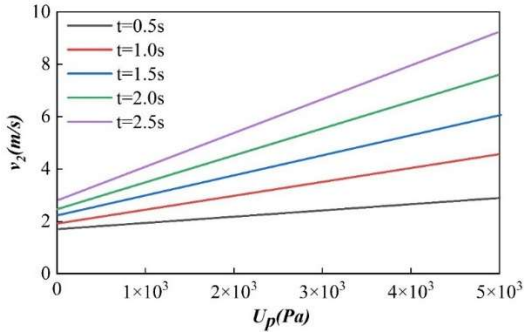

Figure 12: Relationship between velocity and pore water pressure in flow with mixed grains

Figure 13 shows the variation in acceleration at different depths. The vertical load formed by the aggregation of coarse particles on the surface of the debris flow is conducive to the formation of high pore water pressure, which in turn accelerates the liquefaction of particles at the flow interface. It can be seen that under the same pore water pressure conditions, the greater the flow depth, the greater the acceleration, primarily because the increase in sliding force promotes the increase in acceleration. Of course, in debris flows, due to high solid phase volume concentration and uneven particle distribution, the calculated results of vertical velocity distribution may not fully align with the assumptions of the Highbridge model, and velocity does not strictly increase with depth. In fact, the velocity distribution is dispersed, and there may be relatively high velocities in localized areas near the bed surface. However, from a holistic perspective, based on the assumptions of the formula, when a debris flow moves uniformly and stably along a fixed slope, the velocity near the bed surface should be lower, and the calculated results are reasonable. Compared to scenario (a, which includes an overlying coarse-grained layer of fluid), scenario (b, uniform mixing flow) yields a smaller acceleration growth rate. If the debris flow behaves as a homogeneous fluid with good overall integrity, without particle separation, and the pore water pressure changes little during movement, it can theoretically be considered constant. In this case, the pore water pressure does not continue to increase or remain constant but begins to dissipate, thus having no significant accelerating effect on the debris flow.

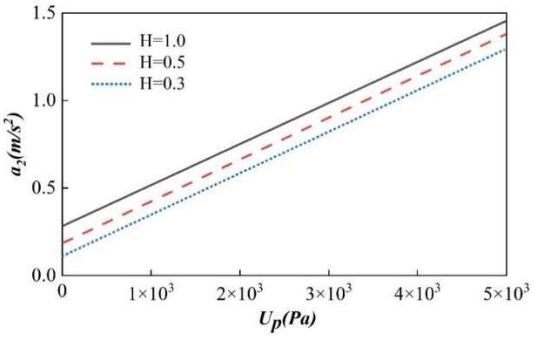

Figure 13: The acceleration of different depths

IV. C. Simulation and analysis of the movement process of mudslides in small streams

IV. C. 1) Analysis of the movement velocity of mudslides in small streams

To quantitatively analyze the movement and deposition characteristics of debris flows, this paper performs post-processing on the numerical simulation results of the Xiahegou debris flow, obtaining the debris flow leading edge velocity curve shown in Figure 14. The period before 280 seconds represents the debris flow's movement phase along the valley, while the period after 280 seconds represents the deposition phase. The results indicate that the Xiaohegou watershed has a willow-leaf-shaped morphology, with a deeply incised “V”-shaped valley. In some areas, the channel is narrow, and when a large amount of fluid enters the main channel, it interacts with the channel deposits, easily causing a “blockage and collapse” phenomenon. It can be observed that from 0 seconds to 6.7 seconds and from 25 seconds to 55 seconds, the local terrain of the Xiahegou River exhibits significant elevation changes, leading to a rapid increase in the velocity of the debris flow's leading edge. Between 92 seconds and 254 seconds, the velocity of the debris flow's leading edge within the main channel fluctuates significantly, reflecting the local “blockage and collapse” effect of the debris flow, as well as the leading edge's movement process of climbing, descending, and climbing again. Between 295 seconds and 320 seconds, it can be observed that after the debris flow exits the gully mouth, the debris flow head experiences a rapid increase in velocity, reaching 5.03 m/s within a short time. This indicates that the terrain at the gully mouth is highly undulating, and the debris flow exiting the gully mouth will cause severe destructive effects on the residential areas at the gully mouth. The mudflow velocity calculated using the formula method at 110m upstream of the gully mouth was 4.25m/s, while the numerical simulation result was 4.85m/s, indicating that the coupled algorithm can provide a relatively accurate prediction of mudflow velocity and has high precision.

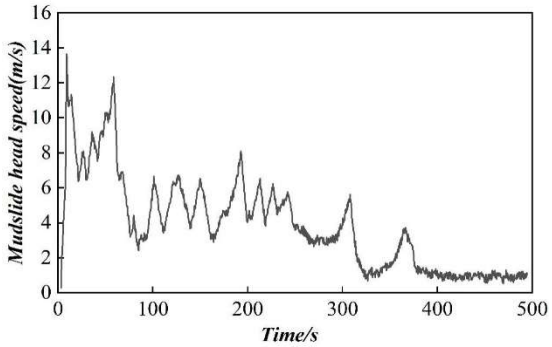

Figure 14: Chart of wind flow

IV. C. 2) Impact of structures on debris flow deposition processes

To quantitatively analyze the impact of structures on debris flows, the debris flow leading edge velocity considering structures was extracted and compared with the debris flow leading edge velocity without considering structures, as shown in Figure 15. The period before 255 seconds represents the debris flow movement stage along the valley, with similar movement trends in both cases. This section primarily focuses on the comparison and analysis of the debris flow mouth sedimentation stage. Under the influence of structures, the debris flow leading velocity slowed to 1.92 m/s, while without considering structures, the debris flow leading velocity exited the valley at 2.74 m/s.

Subsequently, due to terrain effects, both debris flow leading velocities experienced significant increases. The structures reduced the peak flow velocity at the gully mouth from 5.05 m/s to 4.08 m/s. Additionally, the increase in the velocity of the debris flow leading edge when structures are considered is significantly delayed compared to when structures are not considered, and the growth rate is also slower. At 266 seconds, the debris flow head began to accumulate earlier due to the influence of the structures, while without considering the structures, the debris flow head began to accumulate at 270 seconds. It can be seen that the structures reduced the debris flow velocity, causing the debris flow head to accumulate earlier and thereby reducing the debris flow's impact area.

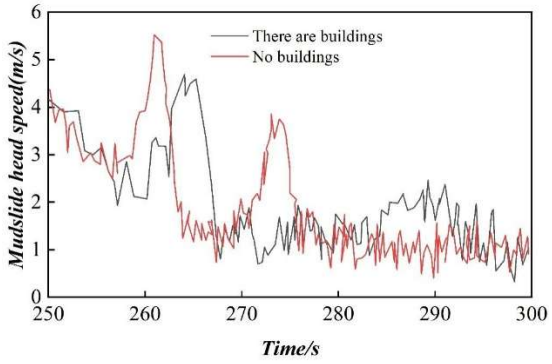

Figure 15: The curve of the wind velocity of the mudslide

V. Conclusion

Mudslides cause enormous losses to humanity, so simulating mudslide movements can help people better understand mudslides and take measures to reduce losses. This paper focuses on realistic modeling and rendering of mudslides, and conducts research in the following areas:

(1) Modeling mudslide movement scenes using the SPH method, where the liquid phase of the mudslide is discretized into Lagrangian particles to solve the Navier-Stokes equations.

(2) Unlike traditional two-dimensional non-Newtonian fluid dam breach problem studies and SPH methods based on deep integration, this paper integrates the HBP constitutive model into the three-dimensional Navier-Stokes equation framework under the SPH format to conduct numerical simulations, enabling the simultaneous acquisition of velocity field distributions and particle distributions in the longitudinal, transverse, and depth directions of the slurry.

(3) During the movement of debris flows, particles undergo continuous adjustments. This process is accompanied by the redistribution of internal stresses, particularly the redistribution of excess pore water pressure, which in turn affects the velocity of the debris flow. Studies on the flowability of debris flows on gentle slopes should not only consider external resistance (reduction in bed resistance) but also focus on the self-acceleration effects between particles.

(4) According to numerical simulation results of debris flows under structures, the structures obstruct the movement of debris flows, reducing the peak flow velocity at the channel mouth from 5.05 m/s to 4.08 m/s, a decrease of 0.97 m/s. Comparative analysis indicates that the structures delayed the movement of the debris flow, reduced its velocity, caused the leading edge of the debris flow fluid to accumulate prematurely, and reduced the extent of the debris flow's impact.

(5) The SPH method is a mesh-free method that uses particle approximation to discretize the computational domain. This is similar to numerical methods under DEM theory. In future research, the SPH method and DEM method can be combined to characterize the interaction between solid and liquid phases. The fluid part can be simulated using the SPH method, while the solid part can be simulated using the DEM method. This can even achieve simulation of debris flow impact on retaining dams and testing dam stability, etc.

References

[1] Zhou, G. G., Li, S., Song, D., Choi, C. E., & Chen, X. (2019). Depositional mechanisms and morphology of debris flow: physical modelling. Landslides, 16, 315-332.

[2] Bo, G. A. O., Jiajia, Z. H. A. N. G., Junchao, W. A. N. G., Long, C. H. E. N., & Dongxu, Y. A. N. G. (2019). Formation mechanism and disaster characteristics of debris flow in the Tianmo gully in Tibet. Hydrogeology & Engineering Geology, 46(5), 144-153.

[3] Wang, L., Chang, M., Dou, X., Ma, G., & Yang, C. (2017). Analysis of river blocking induced by a debris flow. Geofluids, 2017(1), 1268135.

[4] De Haas, T., Densmore, A. L., Stoffel, M., Suwa, H., Imaizumi, F., Ballesteros-Cánovas, J. A., & Wasklewicz, T. (2018). Avulsions and the spatio-temporal evolution of debris-flow fans. Earth-Science Reviews, 177, 53-75.
[5] Zou, Q., Cui, P., He, J., Lei, Y., & Li, S. (2019). Regional risk assessment of debris flows in China—An HRU-based approach. Geomorphology, 340, 84-102.
[6] Kean, J. W., Staley, D. M., Lancaster, J. T., Rengers, F. K., Swanson, B. J., Coe, J. A., ... & Lindsay, D. N. (2019). Inundation, flow dynamics, and damage in the 9 January 2018 Montecito debris-flow event, California, USA: Opportunities and challenges for post-wildfire risk assessment. Geosphere, 15(4), 1140-1163.
[7] Frank, F., Huggel, C., McArdell, B. W., & Vieli, A. (2019). Landslides and increased debris-flow activity: A systematic comparison of six catchments in Switzerland. Earth Surface Processes and Landforms, 44(3), 699-712.
[8] Vargas-Cuervo, G., Rotigliano, E., & Conoscenti, C. (2019). Prediction of debris-avalanches and-flows triggered by a tropical storm by using a stochastic approach: An application to the events occurred in Mocoa (Colombia) on 1 April 2017. Geomorphology, 339, 31-43.
[9] Hirschberg, J., Fatichi, S., Bennett, G. L., McArdell, B. W., Peleg, N., Lane, S. N., ... & Molnar, P. (2021). Climate change impacts on sediment yield and debris-flow activity in an alpine catchment. Journal of Geophysical Research: Earth Surface, 126(1), e2020JF005739.
[10] Zhang, S., & Zhang, L. M. (2017). Impact of the 2008 Wenchuan earthquake in China on subsequent long-term debris flow activities in the epicentral area. Geomorphology, 276, 86-103.
[11] Ma, J., Gao, H., Xu, C., & Qi, S. (2025). Characterization and formation mechanism of the catastrophic flash flood-debris flow hazard triggered by the July 2023 extreme rainstorm in Hantai Gully of Beijing, China. Landslides, 22(3), 877-893.
[12] Michelini, T., Bettella, F., & D'Agostino, V. (2017). Field investigations of the interaction between debris flows and forest vegetation in two Alpine fans. Geomorphology, 279, 150-164.
[13] He, S., Wang, D., Li, Y., & Zhao, P. (2018). Land use changes and their driving forces in a debris flow active area of Gansu Province, China. Sustainability, 10(8), 2759.
[14] Imaizumi, F., Hayakawa, Y. S., Hotta, N., Tsunetaka, H., Ohsaka, O., & Tsuchiya, S. (2017). Relationship between the accumulation of sediment storage and debris-flow characteristics in a debris-flow initiation zone, Ohya landslide body, Japan. Natural Hazards and Earth System Sciences, 17(11), 1923-1938.
[15] Qing-Zhao, Z., Qing, P., Ying, C., Ze-Jun, L., Zhen-Ming, S., & Yuan-Yuan, Z. (2019). Characteristics of landslide-debris flow accumulation in mountainous areas. Heliyon, 5(9).
[16] Li, N., Tang, C., Zhang, X., Chang, M., Shu, Z., & Bu, X. (2021). Characteristics of the disastrous debris flow of Chediguan gully in Yinxing town, Sichuan Province, on August 20, 2019. Scientific Reports, 11(1), 23666.
[17] Kiefer, C., Oswald, P., Moernaut, J., Fabbri, S. C., Mayr, C., Strasser, M., & Krautblatter, M. (2021). A 4000-year debris flow record based on amphibious investigations of fan delta activity in Plansee (Austria, Eastern Alps). Earth Surface Dynamics, 9(6), 1481-1503.
[18] Shen, P., Zhang, L., Chen, H., & Fan, R. (2018). EDDA 2.0: integrated simulation of debris flow initiation and dynamics considering two initiation mechanisms. Geoscientific Model Development, 11(7), 2841-2856.
[19] Long, X. Y., Hu, Y. X., Gan, B. R., & Zhou, J. W. (2024). Numerical simulation of the mass movement process of the 2018 Sedongpu glacial debris flow by using the fluid-solid coupling method. Journal of Earth Science, 35(2), 583-596.
[20] Wang, F., Wang, J., Chen, X., Zhang, S., Qiu, H., & Lou, C. (2022). Numerical simulation of boulder fluid–solid coupling in debris flow: a case study in zhouqu county, gansu Province, China. Water, 14(23), 3884.
[21] dos Santos Corrêa, C. V., Reis, F. A. G. V., do Carmo Giordano, L., Cabral, V. C., Veloso, V. Q., & D'Affonseca, F. M. (2024). Numerical modeling of a high magnitude debris-flow event occurred in Brazil. Natural Hazards, 1-31.
[22] Lee, S., An, H., Kim, M., Lim, H., & Kim, Y. (2022). A simple deposition model for debris flow simulation considering the erosion–entrainment–deposition process. Remote Sensing, 14(8), 1904.
[23] Abraham, M. T., Satyam, N., Pradhan, B., & Tian, H. (2022). Debris flow simulation 2D (DFS 2D): Numerical modelling of debris flows and calibration of friction parameters. Journal of Rock Mechanics and Geotechnical Engineering, 14(6), 1747-1760.
[24] Hu, Y. X., Chen, M. L., & Zhou, J. W. (2019). Numerical simulation of the entrainment effect during mass movement in high-speed debris avalanches. Arabian Journal of Geosciences, 12, 1-15.
[25] Lee, D. H., Lee, S. R., & Park, J. Y. (2019). Numerical simulation of debris flow behavior at Mt. Umyeon using the DAN3D model. Journal of the Korean Society of Hazard Mitigation, 19(3), 195-202.
[26] Cheng, H., Mergili, M., & Huang, Y. (2023). Numerical analysis of debris flow erosion in the mountainous areas affected by the 2008 Wenchuan earthquake using a depth-averaged two-phase model. Natural Hazards, 116(1), 193-212.
[27] Vagnon, F., Kurilla, L. J., Clusaz, A., Pirulli, M., & Fubelli, G. (2022). Investigation and numerical simulation of debris flow events in Rochefort basin (Aosta Valley—NW Italian Alps) combining detailed geomorphological analyses and modern technologies. Bulletin of Engineering Geology and the Environment, 81(9), 378.
[28] Shu, A., Wang, S., Rubinato, M., Wang, M., Qin, J., & Zhu, F. (2020). Numerical modeling of debris flows induced by dam-break using the Smoothed Particle Hydrodynamics (SPH) method. Applied Sciences, 10(8), 2954.
[29] Han, Z., Su, B., Li, Y., Wang, W., Wang, W., Huang, J., & Chen, G. (2019). Numerical simulation of debris-flow behavior based on the SPH method incorporating the Herschel-Bulkley-Papanastasiou rheology model. Engineering Geology, 255, 26-36.
[30] Lanzoni, S., Gregoretti, C., & Stancanelli, L. M. (2017). Coarse-grained debris flow dynamics on erodible beds. Journal of Geophysical Research: Earth Surface, 122(3), 592-614.
[31] Zou, Z., Tang, H., Xiong, C., Su, A., & Criss, R. E. (2017). Kinetic characteristics of debris flows as exemplified by field investigations and discrete element simulation of the catastrophic Jiweishan rockslide, China. Geomorphology, 295, 1-15.
[32] Laigle, D., & Bardou, E. (2022). Mass-movement types and processes: Flow-like mass movements, debris flows and earth flows. Treatise on Geomorphology 2nd Edition, 61-84.
[33] Nagl, G., Hübl, J., & Kaitna, R. (2020). Velocity profiles and basal stresses in natural debris flows. Earth Surface Processes and Landforms, 45(8), 1764-1776.
[34] Lee, S. O., & Song, C. G. (2018). Influence of flow resistance stresses on debris flow runout. Environmental Earth Sciences, 77, 1-15.

[35] Sanvitale, N., & Bowman, E. T. (2017). Visualization of dominant stress-transfer mechanisms in experimental debris flows of different particle-size distribution. Canadian Geotechnical Journal, 54(2), 258-269.
[36] Liu, W., He, S., Chen, Z., Yan, S., & Deng, Y. (2021). Effect of viscosity changes on the motion of debris flow by considering entrainment. Journal of Hydraulic Research, 59(1), 120-135.
[37] Uchida, T., Nishiguchi, Y., McArdell, B. W., & Satofuka, Y. (2021). The role of the phase shift of fine particles on debris flow behavior: an numerical simulation for a debris flow in Illgraben, Switzerland. Canadian Geotechnical Journal, 58(1), 23-34.
[38] Haeri, H., Sarfarazi, V., Zhu, Z., Hedayat, A., & Marji, M. F. (2018). Investigation of the model scale and particle size effects on the point load index and tensile strength of concrete using particle flow code. Struct Eng Mech, 66(4), 445-452.
[39] Kang, C., & Chan, D. (2018). Numerical simulation of 2D granular flow entrainment using DEM. Granular Matter, 20(1), 13.
[40] Albaba, A., Schwarz, M., Wendeler, C., Loup, B., & Dorren, L. (2019). Numerical modeling using an elastoplastic-adhesive discrete element code for simulating hillslope debris flows and calibration against field experiments. Natural Hazards and Earth System Sciences, 19(11), 2339-2358.
[41] Bai, B., Chen, J., Zhang, B., & Wang, H. (2024). Migration trajectories and blocking effect of the fine particles in porous media based on particle flow simulation. AIP Advances, 14(4).
[42] Soham Banerjee, Yves Dubief, Mandar Dewoolkar, Jiarui Chen & Scott Olson. (2025). Inferring apparent Newtonian viscosities of liquefied soils from physical models – Analysis using computational fluid dynamics. Soil Dynamics and Earthquake Engineering,190,109170-109170.
[43] Tao Xiang & Mingjun Li. (2025). Adaptive and stable quartic SPH kernel. Journal of Computational Physics,538,114198-114198.